






# An Improved Method for Soil Moisture Monitoring With Ensemble Learning Methods Over the Tibetan Plateau

Lei He , Member, IEEE, Yuan Cheng , Student Member, IEEE, Yuxia Li , Member, IEEE, Fan Li , Student Member, IEEE, Kunlong Fan , Student Member, IEEE, and Yuzhen Li

**Abstract**—Soil moisture (SM) is a key parameter of the hydrological process, which affects exchanges of water and heat at the land/atmosphere interface. The “trapezoid” (or “triangle”) method has been widely applied to SM monitoring based on the pixel distribution within the thermal and optical remote sensing observations. However, the trapezoid method is a linear empirical model highly related to the retrieval accuracy of the surface temperature. In the article, the moderate-resolution imaging spectroradiometer (MODIS) data were applied to retrieve SM through an improved method over the Tibetan Plateau. The improved method is integrated with the “trapezoid” model and multiple learning techniques, Random Forest (RF) and Extreme Gradient Boosting (XGBoost). Meanwhile, RF and XGBoost were both trained with SM target data (the scale of SM and soil temperature) derived from the Tibetan Plateau observations, and the input variables were derived from MODIS observations. Compared with the SM measured, the results showed the root mean square error, the mean absolute error, and the correlation coefficient of the ensemble retrievals were  $0.046\text{--}0.081\text{ m}^3\text{m}^{-3}$ ,  $0.030\text{--}0.065\text{ m}^3\text{m}^{-3}$ , and  $0.60\text{--}0.87$ , respectively, which is better than that of the separate model. The ideas to implement the combination of traditional inversion algorithms and machine learning methods are helpful for researches in remote sensing fields.

**Index Terms**—Ensemble learning, moderate-resolution imaging spectroradiometer (MODIS), soil moisture (SM), Tibetan plateau (TP), trapezoid model.

## I. INTRODUCTION

AS THE “Third Pole of the Earth,” Tibetan Plateau (TP) is especially sensitive to climate change because of its

Manuscript received July 10, 2020; revised October 25, 2020 and January 18, 2021; accepted February 2, 2021. Date of publication February 9, 2021; date of current version March 12, 2021. This work was supported by the Key Projects of Global Change and Response of Ministry of Science and Technology of China under Grant 2020YFA0608203, in part by the Science and Technology Support Project of Sichuan Province under Grant 2021YFS0335, Grant 2020YFG0296, Grant 2020YFS0338, and Grant 2021YFG0258, and in part by the Fundamental Research Funds for the Central Universities, UESTC under Grant ZYGX2019J064. (Corresponding author: Yuxia Li).

Lei He is with the School of Software Engineering, Chengdu University of Information Technology, The Software Engineering Technology Research Support Center of Informatization Application of Sichuan, Chengdu 610225, China (e-mail: helei197811@foxmail.com).

Yuan Cheng, Yuxia Li, Fan Li, and Kunlong Fan are with the School of Automation Engineering, University of Electronic Science and Technology of China, Chengdu 611731, China (e-mail: shyaabb@163.com; liyuxia@uestc.edu.cn; 1149676921@qq.com; 978901039@qq.com).

Yuzhen Li is with the Department of Big Data, Chengdu Software Development Center, Chengdu 610041, China (e-mail: lily\_lyz2001@126.com).

Digital Object Identifier 10.1109/JSTARS.2021.3058325

special geographical location and high-altitude feature. TP also has a significant impact on the Asian monsoon, the circulation of East Asia, and the land-atmosphere interactions of Global Climate Change (GCC), especially in the process of energy and water cycles [1], [2]. Soil moisture (SM), a key physical parameter in the land surface process, affects the exchange of latent and sensible heat at the land/atmosphere interface [3]–[5]. Monitoring regional SM is significant in the fields of agriculture, hydrology, meteorology, and ecology [6]. However, accurate estimation of SM is still hard to complete for the spatiotemporal heterogeneity, especially for TP.

Generally, SM can be obtained in two ways, field measurements and remote sensing observations. Field measurements can get relatively accurate results, but time-consuming and cost are unable to sustain for large areas. Compared with field measurement, remote sensing methods provide an alternative way with shorter time intervals, different spatial observation scales, and lower costs. Several meteorological satellites, such as the Advanced Scatterometer on EUMETSAT MetOp-A and MetOp-B satellites, the European Soil Moisture and Ocean Salinity Satellite [7], and Soil Moisture Active-Passive Satellite [8], present great possibilities for SM monitoring at a large spatial extend. The remote sensing methods for SM monitoring can be classified into three major groups according to different electromagnetic wavelengths [9].

- 1) Optical methods (wavelengths between  $0.35$  and  $2.5\ \mu\text{m}$ ). The spectral reflectance characteristics of soils are closely related to soil color (species), primary minerals, secondary minerals, water content, organic matter, and texture status. Regression analysis is often used to construct an empirical relationship between reflectance and SM [10].
- 2) Thermal infrared methods (wavelengths between  $3.5$  and  $14\ \mu\text{m}$ ). The soils with different humidity have different thermal inertia, so, the variation of soil surface temperature is also different. Thermal infrared methods usually take thermal inertia [11], [12] or combine surface temperature and vegetation indices to retrieve SM [13]–[15].
- 3) Microwave methods (wavelengths between  $5$  and  $1000\ \text{mm}$ ). Since water and soil components have different dielectric properties, the dielectric constant of the soil-water mixture will increase with SM increasing [16].

Among these three methods, microwave remote sensing (RS) have been widely used in the retrieval

of SM due to the direct relationship between SM and the soil dielectric constant. Microwave methods can be divided into active microwave method and passive microwave method according to different principles. Active microwave uses backscattering coefficient to retrieve SM, while passive microwave mainly uses brightness temperature to estimate SM. Further, many studies are devoted to verifying or improving the retrieved accuracy of SM from microwave data [17]–[20]. Although the microwave method is more widely used in SM retrieval, passive microwave has the disadvantage of low spatial resolutions, and active microwave not only has low temporal resolutions, but also is easily affected by vegetation and soil roughness [21].

Within this context, optical, microwave, and thermal methods are also essential in SM monitoring because they can provide more information. Hence, the development of robust methods plays a key role in SM monitoring.

The trapezoid (or triangle) method has been widely used to estimate SM based on thermal and optical data, because it is easy to operate and requires little ground auxiliary data [22]–[24]. However, the trapezoid method also suffers from two inherent limitations. First, land surface temperature is affected not only by SM but also by ambient atmospheric conditions. Second, these traditional optical-based models are usually empirical or semi-empirical models, which are unable to apply in different regions and times.

Considering the nonlinear correlations between SM and corresponding parameters, machine learning (ML), such as support vector machines (SVMs) [25] and artificial neural networks [26], [27], has been introduced to retrieve SM. However, such ML methods are prone to over-fitting or under-fitting to deal with high-dimensional dataset with poor interpretability. In this article, we improved the trapezoid (or triangle) for SM predictions with ensemble methods [i.e., Extreme Gradient Boosting (XGBoost) and Random Forest (RF)]. The thermal and optical data of moderate-resolution imaging spectroradiometer (MODIS) are the main source data in the research. Due to the heterogeneity of climate and terrain in different regions, the MODIS LST products were calibrated with an RF algorithm to construct the trapezoid (or triangle) model. Meanwhile, XGBoost and RF were trained with vegetation indices derived from MODIS data. SM and temperature measured in TP observatory of the plateau were taken as the expected outputs. Finally, these three models' predictions were combined by ensemble learning method stacking. By combining traditional methods with ML methods, the clear physical meaning of traditional methods and the strong nonlinear fitting capabilities are fully considered and utilized. The prediction results of the integrated algorithm can be helpful to meet the requirements of general applications and proved good potential to produce a high-resolution SM distribution map.

## II. STUDY AREA AND DATA

### A. Study Area

The TP is known as “Roof of the World” and “Third Pole,” which is located between  $26.00^{\circ}$  to  $39.47^{\circ}$ N and  $73.19^{\circ}$  to

$104.47^{\circ}$ E. It extends from the Himalayas in the south to the northern margins of the Kunlun Mountains, Altun Mountains, and Qilian Mountains in the north; and it covers from Pamirs and Karakorum Mountains in the west to the Hengduan Mountains in the east. The TP area is approximately 2.5 million square kilometers. The types of land cover in TP include cultivated land, forests, grasslands, shrubs, wetlands, water bodies, tundra, man-made cover, bare land, glaciers, and permanent snow cover. Grassland, forest, and bare soil are the main land cover types. The precipitation in TP mainly occurs in summer (from May to October), and the average annual precipitation is about 500 mm. Due to the difference in altitude and latitude, the annual average precipitation in the southeast of the plateau can reach 2000 mm, while the average annual precipitation in the northwest is only around 50 mm. The annual average temperature decreases from  $20^{\circ}$ C in the southeast to  $-6^{\circ}$ C in the northwest. TP is not only related to global environmental changes, it is also one of the most sensitive areas affected by global environmental changes due to the complex terrain and climate.

### B. In Situ Measurement

The TP observatory of plateau scale SM and temperature provide representative records of different climatic and terrestrial surface hydrometeorological conditions [28]. Three reference networks (Naqu, Maqu, and Ngari) are available with different climate conditions (see Fig. 1) [29]. Considering that the Ngari network is located in the severe frozen area of the plateau, this article only collected field measurements derived from the Naqu network and Maqu network to build the SM retrieval model. While Ngari network still plays a key role in SM monitoring over TP.

The Maqu Network was established in the northeastern part of the TP in May 2008. The network is located between  $33.5^{\circ}$ – $34.25^{\circ}$ N and  $101.63^{\circ}$ – $102.75^{\circ}$ E. Affected by the monsoon, the climate type of the monitoring network is relatively humid and cold. The Maqu network includes 20 ground measurement sites, covered approximate  $40 \times 80$  km<sup>2</sup>. Most of the measurement sites are installed in valleys, while the rest are located on hills and wetlands. SM and surface temperature are measured every 15 min, and the measurement depths are 0.05, 0.10, 0.20, 0.40, and 0.80 m, respectively.

The Naqu Network was established in the middle of the TP in July 2010, and locates between  $31.0^{\circ}$ – $32.0^{\circ}$ N and  $91.5^{\circ}$ – $92.5^{\circ}$ E. The Naqu area has a cold and semi-arid climate with an average altitude of about 4650 m, covered approximate  $100 \times 100$  km<sup>2</sup>. The Naqu Observation Network has designed three different observation scales: large, medium, and small for different surface hydrological models. The spatial ranges covered are  $1.0^{\circ}$ ,  $0.3^{\circ}$ , and  $0.1^{\circ}$ , respectively. The Naqu network contains 56 ground measurement sites. Most of the ground sites are located in the valleys of the Yellow River and the surrounding hills. The main types of land cover are prairie grass and moss. The SM and surface temperature could be obtained every 15 min, and the measuring depth is 0.05, 0.10, 0.20, and 0.40 m, respectively.

### C. Satellite Measurement

1) *MODIS*: MODIS data are from the sensor equipped with Terra and Aqua satellites, which has 36 spectral channels and the spectrum ranges from 0.4 to 0.14  $\mu\text{m}$ . Compared with other optical satellite data, MODIS has the following advantages.

- 1) Terra and Aqua satellite can transit twice a day in the same area, which makes MODIS data have higher time resolution.
- 2) MODIS sensor has higher sensitivity and quantization accuracy. The radiation resolution can reach 12bit, the temperature resolution can reach 0.03  $^{\circ}\text{C}$ , and the quantization level is higher than other sensors.
- 3) MODIS receives less interference when describing vegetation coverage information because of the narrow band.
- 4) MODIS has an early launch time with abundant data, which can meet the requirements of long-term SM monitoring.

In this article, MODIS cloud-free images MOD11A1 (1-km surface temperature/emissivity daily product), and MOD09A1 (0.5-km surface reflectance 8-day product) were acquired. For the MOD09A1 product, the DN value of each pixel is the optimal value of the observation condition within eight days.

2) *Digital Elevation Model*: The digital elevation model (DEM) is a modeling process for the terrain on the ground. The limited elevation data could be applied to approximate the terrain and provide basic information on the height and characteristics of the earth's surface. The ASTER-GDEM earth electronic terrain data are produced according to the observation results of the TERRA satellite, whose horizontal accuracy and vertical accuracy are 30 and 20 m, respectively, and area covered 99% of Earth's land surface between latitude  $83^{\circ}$  north and  $83^{\circ}$  south. In the research, the applied ASTER-GDEM data are downloaded from the Land Processes Distributed Active Archive Center.<sup>1</sup>

### D. Data Preprocessing

The research collected the measured surface SM and surface temperature from Maqu Network from April 2008 to June 2016 and Naqu Network from August 2010 to October 2016 at the depth of 5 cm. Meanwhile, MODIS data consistent with the ground observation data had been obtained from the Data and Information of Earth Observing System (<https://earthdata.nasa.gov/>). Considering the disturbances of snow and frozen soil, the data were selected only from May to October each year in the research.

The MODIS data were corrected for atmospheric and aerosol processing. All satellite data had been projected to the WGS84 coordinate system and resampled to 1000-m spatial resolution. The preprocessing could be completed in batches with the MODIS Reprojection Tool and ENVI5.3. After removing invalid data, the field measured data are all stored in text form. Further, the field data were programming with Python's GDAL library, synchronizing with the latitude, longitude, and acquired time of the remote sensing data.

<sup>1</sup>[Online]. Available: <https://lpdaac.usgs.gov/>

TABLE I  
CALCULATION FORMULA OF VIS USED IN THIS ARTICLE

VIs	Formulation	References
NDVI	$(R_{b2} - R_{b1}) / (R_{b2} + R_{b1})$	(Tucker <i>et al.</i> , 1980 [31])
SASI	$\beta_{b5}(R_{b2} - R_{b6})$	(Khanna <i>et al.</i> , 2007 [32])
MSAVI	$(2R_{b2} + 1 - \sqrt{(2R_{b2} + 1)^2 - 8(R_{b2} - R_{b1})}) / 2$	(Qiet <i>et al.</i> , 1994 [33])
SIMI	$0.7071\sqrt{(R_{b6})^2 + (R_{b7})^2}$	(Yao <i>et al.</i> , 2011 [34])
NMDI	$(R_{b2} - (R_{b6} - R_{b7})) / (R_{b2} + (R_{b6} - R_{b7}))$	(Wang <i>et al.</i> , 2007 [35])
DDI	$\sqrt{(R_{b1})^2 + (R_{b2})^2} / (1 + \text{NDVI})$	(Qinet <i>et al.</i> , 2010 [36])
GVMI	$((R_{b2} + 0.1) - (R_{b5} + 0.02)) / ((R_{b2} + 0.1) + (R_{b5} + 0.02))$	(Ceccato <i>et al.</i> , 2002 [37])
EVI	$(2.5(R_{b2} - R_{b1})) / (R_{b2} - 6R_{b1} - 7.5R_{b3} + 1)$	(Huete <i>et al.</i> , 1999 [38])
MSI	$R_{b6} / R_{b2}$	(Hunt <i>et al.</i> , 1989 [39])
NDII6	$(R_{b2} - R_{b6}) / (R_{b2} + R_{b6})$	(Hardisky <i>et al.</i> , 1983 [40])
NDII7	$(R_{b2} - R_{b7}) / (R_{b2} + R_{b7})$	(Rahimzadeh <i>et al.</i> , 2009 [41])
NDTI	$(R_{b6} - R_{b7}) / (R_{b6} + R_{b7})$	(Vanet <i>et al.</i> , 1997 [42])
NDWI	$(R_{b2} - R_{b5}) / (R_{b2} + R_{b5})$	(Gao <i>et al.</i> , 1995 [43])
VSDI	$1 - (R_{b6} + R_{b1} - 2R_{b3})$	(Zhang <i>et al.</i> , 2013 [44])

## III. METHODS

### A. Vegetation Indices

Soil is a mixture of a variety of complex substances. The spectral characteristics of soil are closely related to soil color (type), primary minerals, secondary minerals, water content, organic matter, and texture conditions. The relative uniform texture of soil shows an approximate negative correlation between soil spectral reflectance and SM, which laid a theoretical foundation for applying spectral reflectance to monitor SM.

Vegetation Indexes (VIs) are often used to characterize the surface vegetation coverage and growth vitality, which is calculated with land reflectance in different band combinations. Compared with the single-band reflectivity, VIs can enhance the interpretation of remote sensing images, which can reduce the interference from nonvegetation signals while amplifying the vegetation information. VIs has been widely used in the remote sensing retrieval of SM.

Table I shows the 14 VIs related to SM selected from remote sensing literature, where  $R_{bi}$  represents the reflectance of the  $i$ th ( $i = 12 \dots 7$ ) band of MODIS.

In addition, Table I shows that the reflectance of the first seven bands of MODIS, DEM, and reconstructed MODIS LST are also used as initial input features for SM retrieval.

### B. Trapezoid Model

Surface radiant temperature and surface energy fluxes are sensitive to SM and vegetation distribution. When there is lack of water in soil, the plant will close some stomata to reduce the transpiration, which will lead to the decline of latent heat flux, increase of the sensible heat flux, and ultimately increase

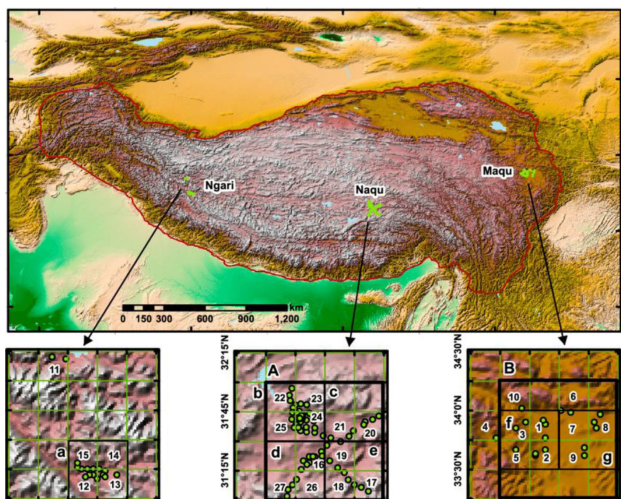


Fig. 1. Location of three regional networks for SM and soil temperature observatory in TP [30].

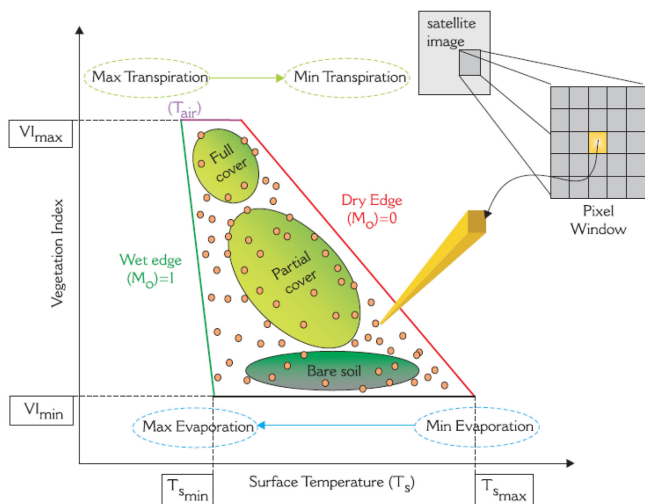


Fig. 2. Theoretical space between surface temperature and VI. [50].

of surface temperature of the blade. Based on the mechanism of surface radiation temperature, SM, and vegetation distribution, some researchers began to use the soil-vegetation-atmosphere transfer model to retrieve the soil water content and evapotranspiration [45]–[47]. However, these surface layer models are always complex and require additional atmospheric parameters, such as surface albedo and wind speed. Price [48] and Carlson *et al.* [49] found that the shape of surface temperature ( $T_s$ ) and vegetation coverage pixel distribution ( $T_s/VI$  scatterplot) will be triangular or trapezoidal for a research area containing a full range of vegetation coverage and SM. For areas with high vegetation coverage,  $T_s$  is not sensitive to SM variations; for bare soil areas, the sensitivity between  $T_s$  and SM variations is increased. The shape of  $T_s/VI$  scatterplot is triangular or trapezoidal (see Fig. 2).

In Fig. 2, the right border of the scatterplot is called the “dry edge,” which is defined by the location of the upper limit of

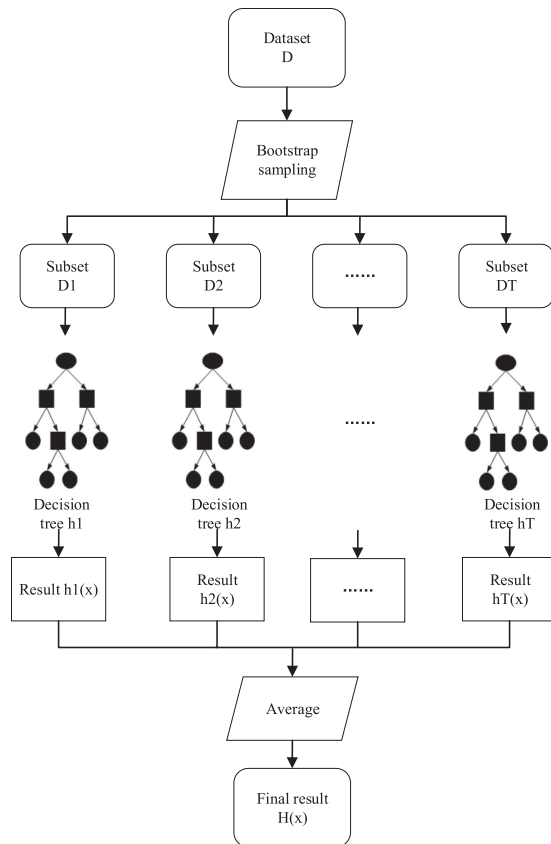


Fig. 3. Structure of RF.

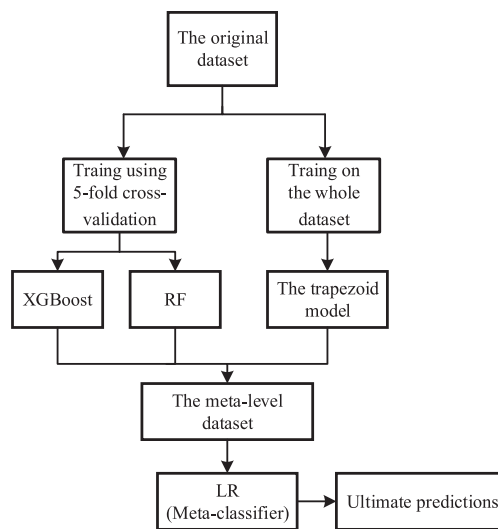


Fig. 4. Structure of the integrated model.

$T_s$  under different vegetation coverage conditions. In addition, the left border of the scatterplot is called the “wet edge,” which is defined by the lower limit of  $T_s$  under different vegetation coverage conditions. For any pixel point inside the trapezoid (or triangle) feature space, the closer to the “dry edge,” the less SM. Otherwise, the closer to the “wet edge,” the higher SM. Surface

evaporation increases with the increase of SM, resulting in a decrease in leaf temperature. But when the vegetation is subjected to water stress, the plant tends to close its stomata to reduce transpiration, resulting in leaf temperature increasing. Based on the triangular or trapezoidal distribution scatterplot, Sandholt *et al.* [51] proposed the Temperature Vegetation Drought Index (TVDI) to measure the relative distance of any pixel points from the dry and wet edges to evaluate the surface SM status. TVDI is defined as follows:

$$\text{TVDI} = \frac{T_S - T_{s\min}}{T_{s\max} - T_{s\min}} \quad (1)$$

where  $T_S$  is the surface temperature corresponding to a certain pixel,  $T_{s\max}$  and  $T_{s\min}$  are the dry and wet edges of the scatterplot.

$$T_{s\max} = a_1 + b_1 \text{NDVI} \quad (2)$$

$$T_{s\min} = a_2 + b_2 \text{NDVI} \quad (3)$$

where  $a_1$  and  $b_1$  are intercept and slope of the “dry edge,”  $a_2$  and  $b_2$  are intercept and slope of the wet edge.

Based on (1)–(3), TVDI can be defined by  $T_S$  and  $VI$

$$\text{TVDI} = \frac{T_S - (a_2 + b_2 \text{NDVI})}{(a_1 - a_2) + (b_1 - b_2) \text{NDVI}} \quad (4)$$

After obtaining TVDI, a linear empirical model of TVDI and SM can be established. It is assumed that TVDI is related to SM, which is due to the change of thermal inertia and evaporative control on the available energy. To improve the prediction of the trapezoid model, Rahimzadeh-Bajgirani *et al.* [24] introduced nonlinear relationship between  $T_s/VI$  and SM. Sun *et al.* [52] proposed a two-stage trapezoid model considering that the vegetation can absorb deep SM to maintain transpiration compared with bare soil. However, these trapezoid models suffer from two inherent limitations. First, the  $T_s/VI$  space is highly correlated with the retrieval accuracy of surface temperature, so it would vary with the high variation of surface temperature. Second, the traditional trapezoid method is always used to constraint the solution for SM (or fluxes) retrievals, and it cannot provide accurate SM predictions.

### C. Ensemble Learning Methods

Focused on quantitative remote sensing, ML only considers simplified models without relevant parameters. Meanwhile, it can also introduce various types of remote sensing data and achieve fusion of multi-source remote sensing data. Traditional ML methods, such as SVM and neural networks, are simple and convenient. However, when dealing with high-dimensional data, over-fitting/under-fitting problems may occur and affect the accuracy of inversion. Ensemble learning could combine multiple single learning models to obtain a unified integrated learning model for more accurate and stable results. Each of these single learning models is called a “weak learner,” and the integrated model ultimately generated uniformly is called a “strong learner.”

1) *Random Forest*: The RF is an ensemble method based on classification and regression tree (CART), which can reduce the risk of overfitting by averaging these trees [53]. The structure of RF model in the article is shown in Fig. 3. During the training period of RF, it first performed sampling with bootstrap in the original training dataset  $D$ . After  $m$  times of sampling, a new training set  $D_1$  with  $m$  samples can be obtained. T-sampling is performed in the same way, and input features  $n \{X_1, X_2 \dots X_n\}$  are randomly selected in each round of sampling. Generally, samples (row) and input features (column) are randomly selected from the original training set  $D$ , and then, new datasets  $T \{D_1, D_2 \dots D_T\}$  can be obtained. Based on each new dataset  $T$ , “weak learners”  $\{h_1, h_2 \dots h_T\}$  can be trained, and the results of each “weak learner” are combined by voting or averaging. In the RS model, the existence of sample perturbations (random row sampling) and attribute perturbations (random column sampling) makes each decision tree trained different, ensuring the diversity of the model. If the decision trees are combined using the average method, the final output result is shown as

$$H(x) = \frac{1}{T} \sum_{i=1}^T h_i(x). \quad (5)$$

2) *Extreme Gradient Boosting*: The XGBoost, proposed by Chen *et al.* [54], is also an ensemble learning approach based on gradient boosting machine. Similar to RF, XGBoost also combines a bunch of CART decision trees to produce a strong learner. The main difference between the two algorithms is that each tree is trained in parallel for the RF algorithm. While for XGBoost, all the decision trees are not independent of each other: The first tree is built on the whole training set, while the second one is built using the training set based on the residuals except for the first tree. In other words, the drawbacks of the first tree are considered in the next training period. The training process is repeated until the stop criterion is met. The ultimate result can be made by summing all the predictions of each tree. The objective function of XGBoost at step  $t$  is shown in (6)

$$\text{Obj}^{(t)} = \sum_i l(y_i, y_i^{(t)}) + \sum_{k=1}^t \Omega(f_k) \quad (6)$$

where  $l$  represents the loss function;  $y_i$  is the  $i$ th expected outputs,  $y_i^{(t)}$  is the prediction given by the  $i$ th sample at step  $t$  in (7);  $\Omega$  is the regularization term in (8)

$$y_i^{(t)} = \sum_{k=1}^t f_k(x_i) \quad (7)$$

$$\Omega(f_k) = \gamma T + \frac{1}{2} \lambda \|\omega\|^2 \quad (8)$$

In the above formulas,  $f_k$  is the  $k$ th decision tree;  $x_i$  is the input variable;  $T$  is the number of leaves and  $\omega$  is the magnitude of leaf weights;  $\gamma$  and  $\lambda$  are the penalty controlling parameters. Detailed computation process of XGBoost can be found in Chen *et al.* [54].

3) *Integrated Model*: Stacking (stacked generalization) is a model ensemble method proposed by Wolpert [55]. The training process of stacking involves two phases. In phase I, several learning algorithms (called base model) are trained on the original training set by applying a procedure similar to k-fold cross-validation. Then, the predictions of each base model are collected to form a new dataset (called the meta-level training dataset). In this dataset, each input parameter corresponds to the expected output parameters (i.e., the real value). In phase II, the meta-level training dataset is used to train an additional algorithm (called meta-model). Similar to training, the test process also includes two phases, and the ultimate predictions are obtained from the meta-model.

The structure of the integrated model proposed in this article is shown in Fig. 4. The base models are the trapezoid model, RF and XGBoost. The meta-model is line regression (LR). Considering the relationship between TVDI and SM, TVDI is introduced for constructing the metadata set to realize the combination of traditional SM inversion methods and ML methods. Compared with stacking, although the trapezoid model is used as the base model, its parameters are still determined by the entire dataset. So, the trapezoid model is fixed throughout the entire training stage. Focused on RF and XGBoost, both are trained with the same dataset in a way similar to five-fold cross-validation. After training, the predictions of the three base models are combined to form a meta-level training dataset, which will be used to train the meta-model (i.e., LR). The ultimate predictions of SM are obtained from LR.

4) *Feature Selection*: For an ML task, eliminating irrelevant features can not only improve the generalization ability but also accelerate the training speed of the model. In the ensemble learning method based on the decision tree, feature importance is often used as the criterion for feature selection. If the time of feature used as an optimal partition attribute is greater, the feature importance is greater.

Except for classification and regression, RF is also used for feature selection in ML models. In the RF model, each decision tree selects the optimal attribute for node division by calculating the Gini value of each feature. The formula for calculating the Gini value  $GI_m$  is shown as

$$GI_m = 1 - \sum_{i=1}^K P_{mi}^2 \quad (9)$$

where  $P_{mi}$  represents the proportion of the  $i$ th sample in the current sample set of node  $m$ , and  $K$  is the number of sample categories in the current data set. If the feature  $X_j$  is selected as the optimal partition attribute of the node  $m$  after calculation, the feature importance of the feature  $X_j$  at the node  $m$  is

$$VIM_{jm}^{\text{gini}} = GI_m - GI_l - GI_r. \quad (10)$$

Among them,  $GI_l$  and  $GI_r$  represent the Gini values of the new nodes  $l$  and  $r$  after the node division, respectively. The feature importance of feature  $X_j$  in the RF model is

$$VIM_j^{\text{gini}} = \sum_{i=1}^T \sum_{m \in M} VIM_{jm}^{\text{gini}}. \quad (11)$$

TABLE II  
PARAMETERS OF RF

Parameter type	Parameter name	Parameter description	Parameter setting
Bagging frame parameter	n_estimators	Decision tree number or maximum number of iterations	600
	bootstrap	use sampling with return or not	True
	criterion	Evaluation standard of node Division	Mse
Decision tree parameter	max_features	Maximum number of features that can be referenced in node partition	None
	max_depth	Maximum depth of decision tree	7
	min_samples_split	The minimum number of samples for internal node subdivision	10

In the above formula,  $M$  represents the set of nodes and the feature  $X_j$  is the optimal partitioning attribute in the decision tree  $i$ , and  $T$  represents the total number of decision trees in the RF. Finally, the importance of the feature  $X_j$  is normalized and the basis for feature selection is defined as follows:

$$VIM_j = \frac{VIM_j^{\text{gini}}}{\sum_{i=1}^n VIM_i^{\text{gini}}}. \quad (12)$$

## RESULTS AND DISCUSSION

### A. Land Surface Temperature Reconstruct

In the research, RF algorithm was applied to reconstruct the MODIS LST products. The parameters of the RF algorithm can be divided into bagging frame parameters and decision tree parameters. Table II shows the main parameters, parameter descriptions, and parameter setting values, respectively.

The RF model is trained with near-infrared band reflectivity and normalized difference vegetation index (NDVI) retrieved from MOD09A1, day and night LST from MOD11A1, and digital elevation data from Aster-GDEM as inputs, and expected outputs are from Tibet-Obs. Among the inputs, NDVI is used here to parameterize the vegetation coverage. Near-infrared band reflectivity is used to parameterize the influence of solar radiation. Further, the elevation is used to reduce the effects of surface characteristics and the location. Land surface temperature is also influenced by SM and precipitation. Focused on the difficulty of coarse spatial resolutions and acquisition, the two factors are not considered in current research.

After the quality control process, total 48 475 point data during May 15, 2008, to October 31, 2015 in Maqu and August 1, 2010, to October 31, 2015, in Naqu are obtained. 80% of the data is used for training, and 20% of the data is used to validate the accuracy of the model. In order to verify the time migration of the RF-based algorithm, a total of 5854 point data of 2016 were applied to test the accuracy of the algorithm. In order to evaluate

TABLE III  
ACCURACY OF THE RECONSTRUCTED SURFACE TEMPERATURE ON THE VERIFICATION SET AND TEST SET

Metrics	Validation dataset	Test dataset (Maqu)	Test dataset (Naqu)
RMSE	2.88	2.68	3.76
MAE	2.00	2.15	2.92
R	0.88	0.79	0.74

the accuracy of such an RF-based model, this article selected root mean square (RMSE), mean absolute error (MAE), and correlation coefficient ( $R$ ) as the accuracy evaluation indicators

$$\text{RMSE} = \sqrt{\frac{1}{N} \sum_{i=1}^N (f_i - y_i)^2} \quad (13)$$

$$\text{MAE} = \frac{1}{N} \sum_{i=1}^N |f_i - y_i| \quad (14)$$

$$R = \frac{\text{Cov}(F, Y)}{\sigma_F \sigma_Y} \quad (15)$$

Table III shows the prediction accuracy of the surface temperature reconstruction algorithm on the verification set and the test set. The reconstructed surface temperature is close to the measured surface temperature, and the two parameters have a high correlation. The surface temperature reconstruction algorithm based on RF can be applied to make improvement of MODIS surface temperature products.

Fig. 5 shows the surface temperature of MOD11A1 during the day, MOD11A1 at night, and the reconstructed surface temperature of the research area in TB. The surface temperature reconstruction algorithm based on RF can supply the missing values of MODIS products. The reconstructed surface temperature value is between MOD11A1 day and night products.

### B. Feature Selection Outcome

In the article, a total of 23 initial input features were used to build the SM inversion model, including the reflectance of the first seven bands of MODIS, reconstructed surface temperature, digital elevation data, and VIs listed in Table I. All the 23 features were applied to train AF model. And the feature importance results are shown after training (see Fig. 6).

The average value of feature importance ( $1/23 \approx 0.0435$ ) was taken as the threshold for feature selection. Finally, 11 features, including LST, DEM, NDVI, NDTI, NDII7, NMDI, EVI, MSAVI, Rb7, NDWI, and GVMI, were used to build SM retrieval models.

### C. SM Retrieval

The synchronization of ground data and RS data can be completed through the coordinates of each station and the date of data acquisition. After quality control processing, a data set of 50 797 samples is obtained. 80% of the total data was used for model training, and 20% of the total data was used for model verification. The number of samples from Maqu networks is

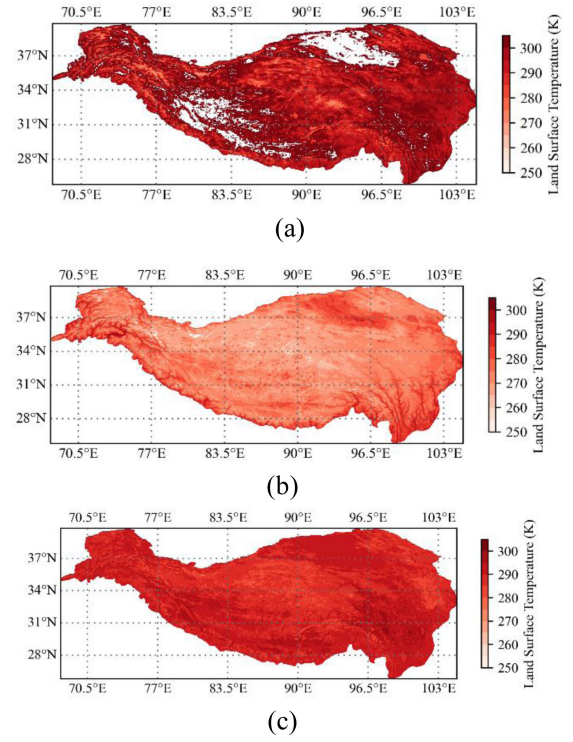


Fig. 5. Land surface temperature of the TB. (a) MOD11A1 LST during the day. (b) MOD11A1 LST during the night. (c) LST after reconstruction.

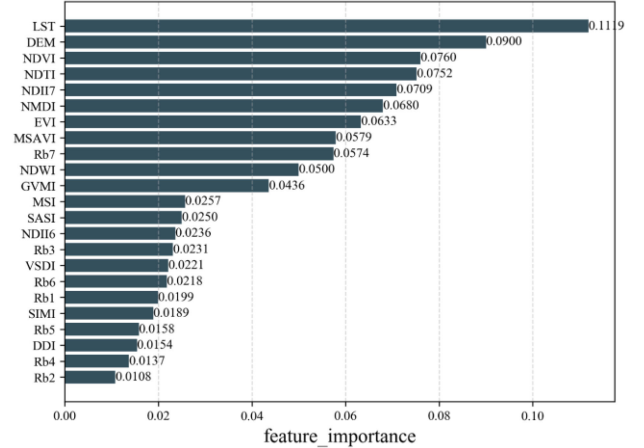


Fig. 6. Feature importance based on RFs.

18 420, and the time range is from May 15, 2008, to October 31, 2015. The number of samples from Naqu networks is 32 377, and the time range is from August 1, 2010, to October 31, 2015. Total 11 initial input features were applied to build the SM inversion model, including the spectral reflectance of the seven bands of MODIS, VIs (NDVI, NDTI, NDII7, NMDI, EVI, MSAVI, NDWI, GVMI), surface temperature, and digital elevation data. In order to evaluate the accuracy of SM inversion results, the research selects RMSE, MAE, and  $R$  as accuracy evaluation indicators. The prediction accuracy comparison of each model on the verification set is shown in Table IV

TABLE IV  
COMPARISON OF PREDICTION ACCURACY OF EACH MODEL ON THE  
VALIDATION SET

Metrics	RF	XGBoost	Stacking
RMSE	0.053	0.052	0.046
MAE	0.035	0.030	0.030
R	0.83	0.85	0.87

TABLE V  
COMPARISON OF PREDICTION ACCURACY OF EACH MODEL IN  
MAQU NETWORK

Metrics	RF	XGBoost	Stacking
RMSE	0.064	0.060	0.058
MAE	0.041	0.049	0.045
R	0.67	0.68	0.74

TABLE VI  
COMPARISON OF PREDICTION ACCURACY OF EACH MODEL IN NAQU NETWORK

Metrics	RF	XGBoost	Stacking
RMSE	0.080	0.081	0.078
MAE	0.064	0.065	0.062
R	0.60	0.62	0.66

Table IV shows that each model has achieved a high inversion accuracy on the validation set. The estimated accuracy of the Stacking model is superior to that of RF and XGBoost, and RMSE is  $0.046 \text{ m}^3\text{m}^{-3}$ , MAE is  $0.030 \text{ m}^3\text{m}^{-3}$ , and R is 0.87. The predicted values have a high correlation to the measured value. The scatter plots of prediction values of these three models versus the field measurement results are shown in Figs. 7 and 8.

Figs. 7 shows that the distribution of scatter plots on the validation set of each model is relatively concentrated, and the estimated results of SM are relatively close to the measured results. When SM is greater than 0.6, the scatterplot distribution of each model is more scattered, and the overall estimated value is lower than the measured value. The reason maybe that SM reaches the soil holding capacity, the spectral reflectance does not decrease with SM increasing. So, the change in the relationship between reflectivity and SM is the main reason for the overall small estimation.

In order to further verify the migration of each model at different times and in different regions, this research collected and collated measured data in 2016 and RS data of Maqu and Naqu networks. Among them, the number of samples from the Maqu network is 490 points, and the data collection time range is from April 1, 2016, to June 23, 2016. The number of samples from the Naqu network is 4343 points, and the data collection time range is from April 1, 2016, to September 18, 2016. Tables V and VI supply the accuracy comparison of each model in networks of Maqu and Naqu, respectively. The retrieval accuracy of the Stacking-based model in Maqu and Naqu is higher than that of RF and XGBoost, and the best prediction accuracy is obtained in Maqu. Finally, RMSE is  $0.058 \text{ m}^3\text{m}^{-3}$ , MAE is  $0.045 \text{ m}^3\text{m}^{-3}$ , and R is 0.74. The accuracy of the models after fusion is better than their base models.

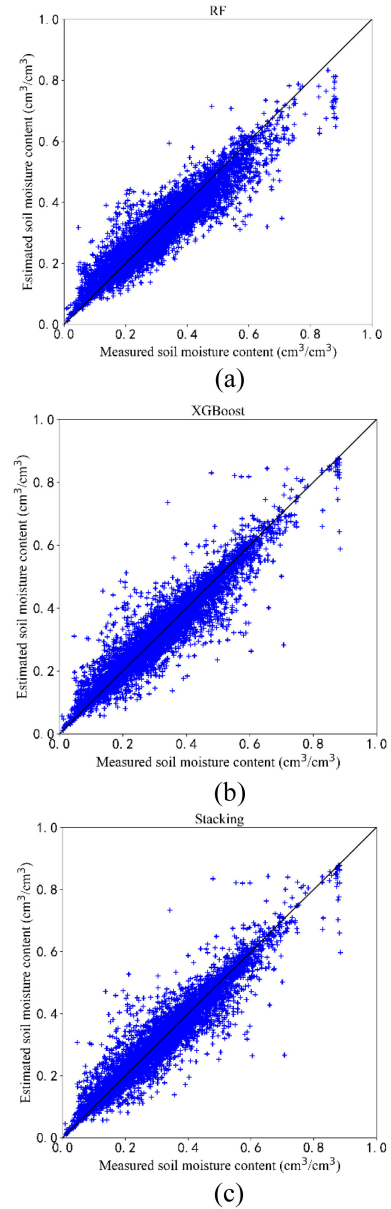


Fig. 7. Scatter plots of SM predictions against field SM measurements. (a) ERT. (b) XGBoost. (c) Multi-model ensemble algorithm based on stacking.

Compared with the inversion accuracy in Tables V and VI, each model in Maqu networks is obviously better than that in Naqu area. The maximum difference of RMSE in different regions is  $0.021 \text{ cm}^3\text{cm}^{-3}$ , and the mean absolute deviation is  $0.023 \text{ cm}^3\text{cm}^{-3}$ . The main reasons for the obvious difference between the two experimental areas are as follows.

- 1) In 2016, the number of stations collected data in Naqu was 28, while only 7 was available in Maqu. The scattered distribution of stations locates in the Naqu area, and more diversified external factors, such as climate and terrain among stations, are complex.
- 2) The data collection time of the Maqu area is from April to June in 2016. So, the distribution of SM is relatively concentrated, and the change range is small at different



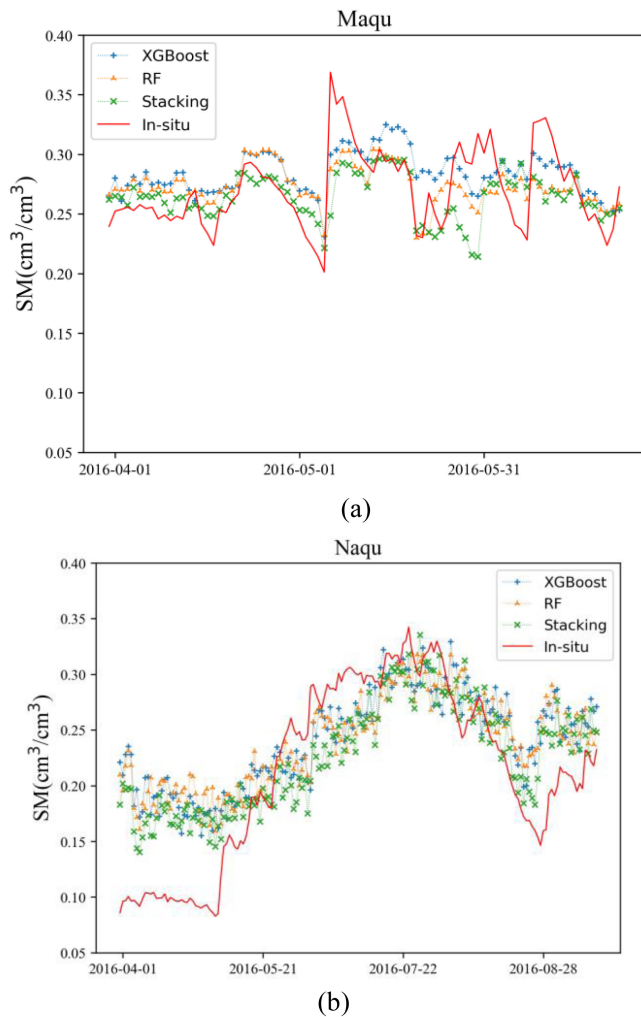


Fig. 8. Time series comparison of SM. (a) Maqu. (b) Naqu.

time. While the data collection time of the Naqu area is from April to October in 2016. So, the distribution range of SM is wide, and the change range is large at different times. Meanwhile, the R-values between the retrieval SM and in-situ SM range from 0.66 to 0.87, which can match the reasonable range of accuracy of remote sensing mapping of large-scale SM [56].

In addition, the research takes the average of SM of each network to further study the trend of SM over time. Fig. 8 shows the time series of SM with the time resolution and the observation scale. The distribution of SM in the Maqu area was relatively concentrated, compared with that in the Naqu area. The SM reaches its maximum from July to August in Naqu. In general, the predictions in Maqu and Naqu agreed well with the measured data over time, and the Stacking model is better than the other two models. Since the number of stations in the Naqu network is larger, which can more accurately reflect the average SM of the current observation network, the retrieval values of SM in the Naqu area are more consistent with the change trends of the measured values. When the SM is low, the retrieval value of each model was higher than the measured value, which shows

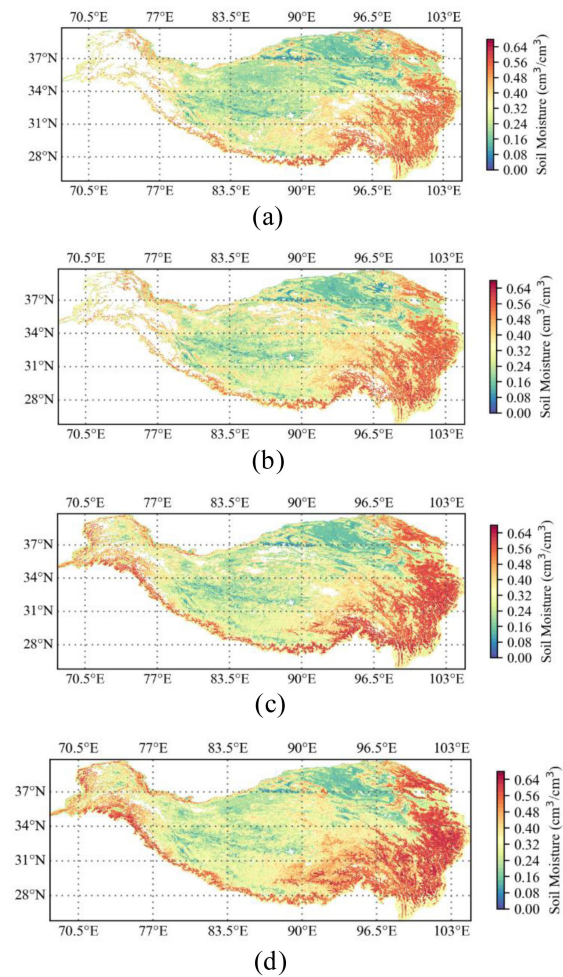


Fig. 9. SM monthly distribution map in the TP. (a) April 2016. (b) May 2016. (c) June 2016. (d) July 2016.

that the current retrieval model cannot accurately reflect extreme drought conditions.

In order to further analyze and verify the spatial distribution of SM in the study area, the research mapped the SM of the entire TP based on the stacking-based algorithm. Fig. 9 shows the SM maps of TP from April to July 2016, with a temporal resolution of 1 month and a spatial resolution of 1 KM.

In general, the SM maps show a decreasing trend from the southeast to the northwest of TP. The SM in the southeast region was significantly higher than that in other regions, while SM in the north region was relatively low. The reason for this spatial distribution is that the land cover type in the southeast area is mainly forests and grasslands, while bare soil occupies the north area. In the Himalayas, there is a high distribution of SM, and the SM of the southern side in the Himalayas is significantly higher than that on the north side.

From April to July, SM in TP has an overall upward trend. In April and May, due to the coverage of glaciers and snow, SM is not available. So, a large number of blank areas appeared in the northwest of TP. In June and July, the ice and snow began to thaw with temperature increasing, and the value of SM in the northwest region also increased. From April to July, SM in the

southern part of TP showed a clear upward trend and reached the maximum value in July. Influenced by the warm and humid air currents carried by the East Asian monsoon, the southern TP has abundant precipitation in summer, which ultimately leads to higher SM in the southern region. The results show that the SM maps of TP have a good agreement with its topography and climate distribution.

Compared with other SM retrieval algorithms based on ML [57], the research made an improvement for reflecting the spatial dynamic changes of SM. In addition, compared with AMSRE, ASCAT, ERA-Interim SM products, and other SM retrieval algorithms based on microwave data [58], the SM map obtained in the research has higher spatial resolution and spatial continuity. Overall, the stacking method shows a good potential to produce high-resolution SM maps. However, due to the lack of measured data in other regions, the transferability of the model has yet to be evaluated. Further work may be directed toward a more robust evaluation with more datasets.

## V. CONCLUSION

In this article, we explored the potential application of remote sensing data for estimating SM in TP using ensemble learning methods. High-resolution multi-spectral imagery, in combination with ground sampling, provided sufficient information to accurately estimate the spatial distribution of SM.

An SM retrieval algorithm that combined the traditional method (the trapezoid method) and ensemble learning methods (i.e., XGBoost and RF) by stacking technology is proposed. In order to improve the reliability of the trapezoid method, we first reconstructed the MODIS land surface temperature product, and then, part of the interference caused by vegetation and terrain was eliminated. Finally, the accuracy and continuity of the product were improved. In addition, the RF was applied in the feature selecting process of SM-related parameters. For selecting parameters with higher feature importance, we trained and tested SM retrieval models of RF and XGBoost, respectively. Finally, we integrated and retrained the results of the RF, XGBoost, and trapezoid methods based on stacking and obtained more accurate SM predictions.

The prediction accuracy assessed by comparison with the *in situ* measurements, RMSE, MAE, and correlation of the ensemble retrievals were 0.046–0.081, 0.030–0.065, and 0.60–0.87, respectively. Results indicate that the SM inversion model based on the extreme random tree has stronger nonlinear expression ability and can introduce more input parameters compared with the empirical model. Compared with traditional ML methods such as SVM and neural networks, extreme random tree can obtain better inversion precision on a small sample set by combining several “weak learners” into “strong learners.” Compared with the RF, the extreme random tree can reduce the variance and model bias and achieve better integration effects. So, the algorithm proposed in this article can achieve good accuracy and be applied for regional SM monitoring. Though the region-specific trained ensemble models in the research are unable to be used immediately in another location, the ideas to implement the combination of traditional inversion algorithms and ML

methods are helpful to the research of information extraction from remote sensing images.

## ACKNOWLEDGMENT

Yuxia Li represents all the authors to thank the reviewers for their constructive comments and kind help to improve the manuscript. Lei He would like to thank the team of Cunjie Zhang of National Climate Center for the work and experiment environment they supplied, the team of Jiancheng Shi of Aerospace Information Research Institute, Chinese Academy of Science, for the remote sensing experiment in Shandian river, NASA Data form <https://earthdata.nasa.gov>.

## REFERENCES

- [1] M. Y. Ma, S. Liu D, B. Su Z, L. Z. Li, M. Menenti, and M. Wang J, “Land surface variables and vegetation variables estimated from satellite remote sensing over inhomogeneous land surface of the northern Tibetan plateau,” *Chin. J. Atmos. Sci.*, vol. 28, no. 1, pp. 23–31, 2004.
- [2] Y. M. Ma, S. C. Kang, L. P. Zhu, B. Q. Xu, L. D. Tian, and T. D. Yao, “Tibetan observation and research Platform- Atmosphere–land interaction over a heterogeneous landscape,” *Bull. Amer. Meteorological Soc.*, vol. 89, pp. 1487–1492, 2008.
- [3] P. C. D. Milly and K. A. Dunne, “Sensitivity of the global water cycle to the water-holding capacity of Land,” *J. Climate*, vol. 7, no. 4, pp. 506–526, 1994.
- [4] R. D. Koster *et al.*, “Regions of strong coupling between soil moisture and precipitation,” *Science*, vol. 305, pp. 1138–1140, 2004.
- [5] T. E. Ochsner *et al.*, “State-of-the-art in large-scale soil moisture monitoring,” *Soil Sci. Soc. Amer. J.*, vol. 77, pp. 1888–1919, 2013.
- [6] Y. H. Kerr *et al.*, “The SMOS mission: New tool for monitoring key elements of the global water cycle,” *Proc. IEEE*, vol. 98, no. 5, pp. 666–687, May 2010.
- [7] H. Kerr, P. Waldteufel, J. P. Wigneron, J. Martinuzzi, J. Font, and M. Berger, “Soil moisture retrieval from space: The soil moisture and ocean salinity (SMOS) mission,” *IEEE Trans. Geosci. Remote Sens.*, vol. 39, no. 8, pp. 1729–1735, Aug. 2001.
- [8] D. Entekhabi *et al.*, “The soil moisture active passive (SMAP) mission,” *Proc. IEEE*, vol. 98, no. 5, pp. 704–716, May 2010.
- [9] S. Morteza *et al.*, “A linear physically-based model for remote sensing of soil moisture using short wave infrared bands,” *Remote Sens. Environ.*, vol. 164, pp. 66–76, 2015.
- [10] L. Wang and J. J. Qu, “Satellite remote sensing applications for surface soil moisture monitoring: A review,” *Front. Earth Sci. China*, vol. 3, no. 2, pp. 237–247, 2009.
- [11] W. W. Verstraeten, F. Veroustraete, C. J. van der Sande, I. Grootaers, and J. Feyen, “Soil moisture retrieval using thermal inertia, determined with visible and thermal spaceborne data, validated for European forests,” *Remote Sens. Environ.*, vol. 101, pp. 299–314, 2006.
- [12] Y. Lu *et al.*, “Accounting for soil porosity improves a thermal inertia model for estimating surface soil water content,” *Remote Sens. Environ.*, vol. 212, pp. 79–89, 2018.
- [13] C. Wang *et al.*, “Evaluating soil moisture status in China using the temperature–vegetation dryness index (TVDI),” *Can. J. Remote Sens.*, vol. 30, no. 5, pp. 671–679, 2004.
- [14] J. Xin *et al.*, “Combining vegetation index and remotely sensed temperature for estimation of soil moisture in China,” *Int. J. Remote Sens.*, vol. 27, no. 10, pp. 2071–2075, 2006.
- [15] S. N. Goward, Y. Xue, and K. P. Czajkowski, “Evaluating land surface moisture conditions from the remotely sensed temperature/vegetation index measurements: An exploration with the simplified simple biosphere model,” *Remote Sens. Environ.*, vol. 79, pp. 225–242, 2002.
- [16] L. Zhu *et al.*, “A multi-frequency framework for soil moisture retrieval from time series radar data,” *Remote Sens. Environ.*, vol. 235, 2019, Art. no. 111433.
- [17] H. Ma *et al.*, “Satellite surface soil moisture from SMAP, SMOS, AMSR2 and ESA CCI: A comprehensive assessment using global ground-based observations,” *Remote Sens. Environ.*, vol. 231C, 2019, Art. no. 111215.
- [18] X. Fan *et al.*, “SMAP underestimates soil moisture in vegetation-disturbed areas primarily as a result of biased surface temperature data,” *Remote Sens. Environ.*, vol. 247, 2020, Art. no. 111914.

- [19] Z. Wei *et al.*, “Downscaling SMAP soil moisture estimation with gradient boosting decision tree regression over the Tibetan plateau,” *Remote Sens. Environ.*, vol. 225, 2019, Art. no. 30–44.
- [20] Q. Yan, W. Huang, S. Jin, and Y. Jia, “Pan-tropical soil moisture mapping based on a three-layer model from CYGNSS GNSS-R data,” *Remote Sens. Environ.*, vol. 247, 2020, Art. no. 111944.
- [21] S. Sánchez-Ruiz *et al.*, “Combining SMOS with visible and near/shortwave/thermal infrared satellite data for high resolution soil moisture estimates,” *J. Hydrol.*, vol. 516, pp. 273–283, 2014.
- [22] D. Zhang *et al.*, “Surface soil water content estimation from thermal remotesens. Based on the temporal variation of land surface temperature,” *Remote Sens.*, vol. 6, no. 4, pp. 3170–3187, 2014.
- [23] R. R. Nemani and S. W. Running, “Estimation of regional surface resistance to evapotranspiration from NDVI and Thermal-IR AVHRR Data,” *J. Appl. Meteorol.*, vol. 28, no. 4, pp. 276–284, 1989.
- [24] P. Rahimzadeh-Bajgiran *et al.*, “Estimation of soil moisture using optical/thermal infrared remote sensing in the Canadian prairies,” *ISPRS J. Photogramm. Remote Sens.*, vol. 83, pp. 94–103, 2013.
- [25] M. K. Gill *et al.*, “Soil moisture prediction using support vector machines,” *J. Amer. Water Res. Assoc.*, vol. 42, no. 4, pp. 1033–1046, 2006.
- [26] L. Hassan-Esfahani *et al.*, “Assessment of surface soil moisture using high-resolution multi-spectral imagery and artificial neural networks,” *Remote Sens.*, vol. 7, no. 3, pp. 2627–2646, 2015.
- [27] J. Kolassa *et al.*, “Estimating surface soil moisture from SMAP observations using a neural network technique,” *Remote Sens. Environ.*, vol. 204, pp. 43–59, 2017.
- [28] K. Yang *et al.*, “A multiscale soil moisture and freeze–thaw monitoring network on the third pole,” *Bull. Amer. Meteorological Soc.*, vol. 94, no. 12, pp. 1907–1916, 2013.
- [29] Z. Su *et al.*, “The Tibetan plateau observatory of plateau scale soil moisture and soil temperature (Tibet-Obs) for quantifying uncertainties in coarse resolution satellite and model products,” *Hydrol. Earth Syst. Sci.*, vol. 15, no. 7, pp. 2303–2316, 2011.
- [30] Z. Qiang *et al.*, “Evaluation of remotely sensed and reanalysis soil moisture against in situ observations on the Himalayan-Tibetan plateau,” *J. Geophysical Res., Atmos.*, vol. 123, pp. 7132–7148, 2018.
- [31] C. J. Tucker, “Remote sensing of leaf water content in the near infrared,” *Remote Sens. Environ.*, vol. 10, no. 1, pp. 23–32, 1980.
- [32] S. Khanna *et al.*, “Development of angle indexes for soil moisture estimation, dry matter detection and land-cover discrimination,” *Remote Sens. Environ.*, vol. 109, no. 2, pp. 154–165, 2007.
- [33] A. R. Huete, “A soil-adjusted vegetation index,” *Remote Sens. Environ.*, vol. 27, no. 3, pp. 119–126, 1988.
- [34] Y. A. O. Yun Jun *et al.*, “Retrieval of soil moisture based on MODIS shortwave infrared spectral feature,” *J. Infrared Millim. Waves*, vol. 30, no. 1, pp. 9–14, 2011.
- [35] L. Wang and J. J. Qu, “NMDI: A normalized multi-band drought index for monitoring soil and vegetation moisture with satellite remote sensing,” *Geophys. Res. Lett.*, vol. 34, 2007, Art. no. L20405.
- [36] Q. Qin *et al.*, “A two-dimensional spectral space-based model for drought monitoring and its re-examination,” in *Proc. IEEE Geosci. Remote Sens. Symp.*, 2010, pp. 3869–3872.
- [37] P. Ceccato *et al.*, “Designing a spectral index to estimate vegetation water content from remote sensing data: Part 1: Theoretical approach,” *Remote Sens. Environ.*, vol. 82, no. 2–3, pp. 188–197, 2002.
- [38] A. Huete, “A comparison of vegetation indices over a global set of TM images for EOS-MODIS,” *Remote Sens. Environ.*, vol. 59, no. 3, pp. 440–451, 1997.
- [39] E. R. Hunt and B. N. Rock, “Detection of changes in leaf water content using near- and middle-infrared reflectances,” *Remote Sens. Environ.*, vol. 30, no. 1, pp. 43–54, 1989.
- [40] M. A. Hardisky, V. Klemas, and R. M. Smart, “The influence of soil salinity, growth form, and leaf moisture on the spectral reflectance of spartina alternifolia canopies,” *Photogramm. Eng. Remote Sens.*, vol. 49, pp. 77–83, 1983.
- [41] P. R. Bajgiran *et al.*, “MODIS vegetation and water indices for drought assessment in semi-arid ecosystems of Iran,” *J. Agricultural Meteorol.*, vol. 65, no. 4, pp. 349–355, 2009.
- [42] V. Deventer *et al.*, “Using thematic mapper data to identify contrasting soil plains and tillage Practices,” *Photogramm. Eng. Remote Sens.*, vol. 63, no. 1, pp. 87–93, 1997.
- [43] B. C. Gao, “NDWI—A normalized difference water index for remote sensing of vegetation liquid water from space,” *Remote Sens. Environ.*, vol. 58, pp. 257–266, 1996.
- [44] N. Zhang *et al.*, “VSDI: A visible and shortwave infrared drought index for monitoring soil and vegetation moisture based on optical remote sensing,” *Int. J. Remote Sens.*, vol. 34, no. 13, pp. 4585–4609, 2013.
- [45] T. N. Carlson *et al.*, “Satellite estimation of the surface energy balance, moisture availability and thermal inertia,” *J. Appl. Meteorol.*, vol. 20, no. 1, pp. 67–87, 1981.
- [46] B. Seguin and B. Itier, “Using midday surface temperature to estimate daily evaporation from satellite thermal IR data,” *Int. J. Remote Sens.*, vol. 4, no. 2, pp. 371–383, 1983.
- [47] P. J. Wetzel, D. Atlas, and R. H. Woodward, “Determining soil moisture from geosynchronous satellite infrared data: A feasibility study,” *J. Appl. Meteorol.*, vol. 23, no. 3, pp. 375–391, 1984.
- [48] J. C. Price, “Using spatial context in satellite data to infer regional scale evapotranspiration,” *IEEE Trans. Geosci. Remote Sens.*, vol. 28, no. 5, pp. 940–948, Sep. 1990.
- [49] T. N. Carlson, R. R. Gillies, and E. M. Perry, “A method to make use of thermal infrared temperature and NDVI measurements to infer surface soil water content and fractional vegetation cover,” *Remote Sens. Rev.*, vol. 9, pp. 161–173, 1994.
- [50] G. Petropoulos *et al.*, “A review of Ts/VI remote sensing-based methods for the retrieval of land surface energy fluxes and soil surface moisture,” *Prog. Phys. Geogr.*, vol. 33, no. 2, pp. 224–250, 2009.
- [51] I. Sandholt, K. Rasmussen, and J. Andersen, “A simple interpretation of the surface temperature/vegetation index space for assessment of surface moisture status,” *Remote Sens. Environ.*, vol. 79, no. 2–3, pp. 213–224, 2002.
- [52] H. Sun, “Two-stage trapezoid: A new interpretation of the land surface temperature and fractional vegetation coverage space,” *IEEE J. Sel. Topics Appl. Earth Observ. Remote Sens.*, vol. 9, no. 1, pp. 336–346, Jan. 2016.
- [53] L. Breiman, “Random forests,” *Mach. Learn.*, vol. 45, pp. 5–32, 2001.
- [54] T. Chen and C. Guestrin, “XGBoost: A scalable tree boosting system,” *Proc. 22nd ACM SIGKDD Int. Conf. Knowl. Discov. Data Mining*, vol. 13–17, pp. 785–794, 2016.
- [55] H. D. Wolpert, “Stacked generalization,” *Neural Netw.*, vol. 5, no. 2, pp. 241–259, 1992.
- [56] D. Entekhabi *et al.*, *SMAP Handbook—Soil Moisture Active Passive: Mapping soil Moisture and Freeze/Thaw from Space*. Pasadena, CA: JPL Publication, 2014.
- [57] J. Im, S. Park, J. Rhee, J. Baik, and M. Choi, “Downscaling of AMSR-E soil moisture with MODIS products using machine learning approaches,” *Environ. Earth Sci.*, vol. 75, 2016, Art. no. 1120.
- [58] Y. Zeng *et al.*, “Blending satellite observed, model simulated, and in situ measured soil moisture over Tibetan plateau,” *Remote Sens.*, vol. 8, pp. 268, 2016.



**Lei He** (Member, IEEE) received the B.S. degree from Dalian Maritime University, Dalian, China, in 2001, the M.S. degree in geography information system from Chengdu University of Technology, Changdu, China, in 2010, and the Ph.D. degree from the University of Electronic Science and Technology of China, Chengdu, China, in 2016.

His research interests include microwave remote sensing, image processing, and deep learning.

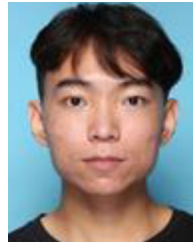


**Yuan Cheng** (Student Member, IEEE) was born in Sichuan Province in 1996. He received the B.S. degree from the University of Electronic Science and Technology, Chengdu, China. He is currently working toward the master’s degrees at the University of Electronic Science and Technology of China, Chengdu, China.



**Yuxia Li** (Member, IEEE) was born in Henan Province, in 1979. She received the B.S. degree from Anhui University of Science Technology, Huainan, China, in 2001, the M.S. and Ph.D. degrees from Chengdu University of Technology, Chengdu, China, in 2004 and 2007, respectively.

Her research interests include remote sensing, image processing, deep learning, and quantitate inversion.



**Kunlong Fan** (Student Member, IEEE) received the B.S. degree from the University of Electronic Science and Technology of China, Chengdu, China, in 2017, where he is currently working toward the master's degrees.



**Fan Li** was born in Shanxi Province in 1996. She received the B.S. degree from the University of Electronic Science and Technology of China, Chengdu, China, where she is currently pursuing her master's degrees.



**Yuzhen Li** was born in Henan Province, China, in 1982. She received the master's degree from Chengdu University of Technology, Chengdu, China.

Her research interests include remote sensing and GIS.